ISSN: 2454-9940

INTERNATIONAL JOURNAL OF APPLIED SCIENCE ENGINEERING AND MANAGEMENT

E-Mail :
editor.ijasem@gmail.com
editor@ijasem.org

www.ijasem.org

INTERNATIONAL JOURNAL OF APPLIED SCIENCE ENGINEERING AND MANAGEMENT

ISSN 2454-9940

www.ijasem.org

Vol 19, Issue 2, 2025

Optimized EV Charging with Fuzzy Logic-Controlled High Current Density DC-DC Converters

[1] B.Rambabu, [2] Amidala Aishwarya, [3] Adavala Raghu Vamsi, [4]Kuruba Shiva,[5] Talupula Reddy Lakshmi, [6] Kavalidoralu Charan Kumar,

[2,3,4,5,6] Student, Department of EEE, Ananthalakshmi Institute of Technology and Sciences, Itikalapalli, Near Sk University, Ananthapur.

[1] Assistant Professor, Department of EEE, Ananthalakshmi Institute of Technology and Sciences, Itikalapalli, Near Sk University, Ananthapur.

ABSTRACT

The environmental benefits of electric cars (EVs) are driving their rising popularity in the automotive industry. Having a dependable, efficient, and cost-effective battery charger is vital for electric cars since they control their power from the rechargeable battery. The charger must give a consistent needed output for the battery of the specific EV. This study introduces a DC-DC converter that uses a modified PI controller. It shortens the charging time of a given lithium-ion battery system by producing the necessary output voltage and high current density with almost no overshoot. In addition to reducing active-switch power loss, the suggested approach also reduces junction temperature, which extends the converter's service life. Both ideal and non-ideal circumstances are used to conduct the study of the proposed converter. Additionally, we have examined the junction temperature and power loss of the active switches. We have analysed the performance of total power loss and temperature increase, and created dc and ac side inductors that are both effective and inexpensive. According to the findings, the suggested converter is capable of keeping the total harmonic distortion at approximately 0.46% and the power factor at around 90%, both of which are optimal for the current flowing through the high-density load. Additionally, the dc-dc converter's dependability is assessed. Additionally, a hardware prototype has been put in place to ensure its suitability for charging electric vehicle batteries. AC-DC converter, isolated ac-dc converter, power factor correction, MOSFET thermal analysis, state-space representation of converter, electric car battery charger, lithium-ion battery charger, and modified PI controller are all terms in the index.

INTRODUCTION

One of the crucial and complex systems that provides electricity to electric vehicles (EVs) is the rechargeable battery. Electric vehicle (EV) battery chargers must be efficient, dependable, and cost-effective. To meet the need, an AC-DC converter is necessary. the numbers1,2,3,4, and 5. You may get an isolated or non-isolated AC-DC converter. increased power loss will occur in the non-isolated system because the active switch and diode are subjected to increased stress. Because of this, the temperature will rise, which might pose a safety risk due to the lack of isolation. Alternatively, in a completely isolated system, the active switch and diode may be subject to less strain, as the voltage can be reduced to meet the requirement, resulting in reduced power loss and lower temperatures at the junction of these devices. The added benefit of this setup is the increased safety factor. Increase the system's overall dependability as a result [6]. The power factor and total harmonic distortion (THD) are both negatively impacted when the AC-DC operation is carried out using a traditional diode rectifier, which results in increased power loss. A complex and expensive method may be used to preserve the PFC tropology. at numbers 7, 8, 9, 10, 11, 12, 13, 14, 15, 16, 17, and 18. A low-frequency coupled inductor (LCL) filter and two diodes are part of an AC-DC converter that has been used to eliminate it [19], [20], [21], [22]. After then, the state of the lithium-ion battery will dictate if voltage regulation is necessary. A DC-DC converter with a closed-loop design may do this. The active switches of a traditional closed-loop DC-DC converter consume a lot of power, which might shorten the system's lifespan. Power loss owing to conduction, switching, and leakage accounts for the majority of the power loss in traditional closed-loop DC-DC converters [23]. Furthermore, the lithium-ion battery may be malfunctioning due to the overshoot at the output voltage and current [24]. In order to overcome this, we repurposed an MPI controller from our earlier work and made some adjustments; this controller helps to decrease conduction power loss, switching power loss, leakage power loss, and overshoot at the output voltage and current [25], [26]. Furthermore, the present prosecution has also been enhanced. As a result, the overall power loss will be reduced without compromising the switching frequency, which aids in keeping passive components small.

INTERNATIONAL JOURNAL OF APPLIED SCIENCE ENGINEERING AND MANAGEMENT
ISSN 2454-9940
www.ijasem.org
Vol 19, Issue 2, 2025

The active switch takes care of the thermal management heatsink, which raises the surface area in relation to the ambient temperature, therefore keeping the junction temperature constant. references [27], [28]. A cost-effective, efficient, and dependable AC-DC converter for charging the lithium-ion battery pack of electric vehicles is introduced in this work. The converter, power loss, and MOSFET junction temperature may all be examined under three distinct scenarios. The outcome of the hardware prototype is also included at the conclusion to support the recommended prosecution.

PROPOSED SYSTEM

Figure 1 shows the suggested system. Power is supplied to the load by the single-phase ac source. For filtering reasons, the LCL network has been designated to be next to the AC source. You may use it to control the power factor and THD as well. The linked inductor's main side may have its ac flow controlled by the two diodes D5 and D6. It is possible to get the rippling dc by connecting the inductor to its secondary side. R3, R4, C3, and C4 all have a role in dampening dc ripples. Subsequently, the dc output voltage is adjusted by the four metal-oxide-semiconductor field-effect transistors (MOSFETs) M1, M2, M3, and M4. To keep the dc flow going, there are four more diodes: D1, D2, D3, and D4. For purposes of storing and filtering, components such as L1, L2, and C1 are accountable. For safety reasons, two fuses, F1 and F2, are designated. In the end, the 48V 100Ah Lithium-Ion battery was used as the load.

AC-DC SYSTEM WITH LCL FILTER

Because single-phase ac changes the phase, this system will exhibit two distinct modes, which will be detailed below. Chapter Four: Mode One This mode occurs at a supply voltage of 0 to 180 volts, with L3, L4, D5, and L5 in conduction mode and D6 in non-conduction mode, leading to a positive voltage at L7 (as shown in Figure 2a). The Second Mode This mode would occur at a supply voltage of 180◦-360◦, with L6, D6, L4, and L3 in conduction mode and D5 in non-conduction mode, once again producing a positive voltage at L7, as shown in Figure 2(b).

DESIGN AND ANALYSIS OF LCL FILTER

The grid current can be estimated based on equation 1.

$$I_{Grid} = \frac{\sqrt{2} \times P_{Load}}{V_{AC}} A \qquad (1)$$

The required inductance can be computed using equation 2.

$$L = \frac{x_L}{2 \times \pi \times f_{AC}} H \qquad (2)$$

where, x_L = Inductor reactance = $2\pi fL$

The L3 and L4 will be half of the inductance that has been calculated.

The ac side capacitance can be calculated as

$$C2 = \frac{1\% \times P_{Load}}{2 \times \pi \times f_{AC} \times V_{AC}^2} F \qquad (3)$$

INTERNATIONAL JOURNAL OF APPLIED SCIENCE ENGINEERING AND MANAGEMENT
ISSN 2454-9940
www.ijasem.org
Vol 19, Issue 2, 2025

The resonant frequency can be computed as

$$F_r = \frac{1}{2 \times \pi \times \sqrt{\frac{L3 \times L4}{L3+L4} \times C2}} Hz \quad (4)$$

The damping resistance can be calculated as

$$Rd = \frac{1}{6 \times \pi \times F_r \times C2} ohm \quad (5)$$

where, f_{AC} = Grid frequency, P_{Load} = Filter load power.

The designed filter frequency response can be analyzed based on the transfer function and given herewith.

$$SYS(s) = \frac{Rd \times C2s + 1}{L3 \times L4 \times C2s^3 + (L3 + L4) \times Rd \times C2s^2 + (L3 + L4)\, s} \quad (6)$$

Figure 3 displays the bode plot, which was produced after modifying the aforementioned equations. The stability and the results of the planned filter's frequency response are shown in the figure. The overall response is smoothed and the spike associated with the system is minimized after adding the damping resistor; nevertheless, spikes do occur when the resistor is not present. Because the damping resistor is included into the intended filter, it becomes more stable.

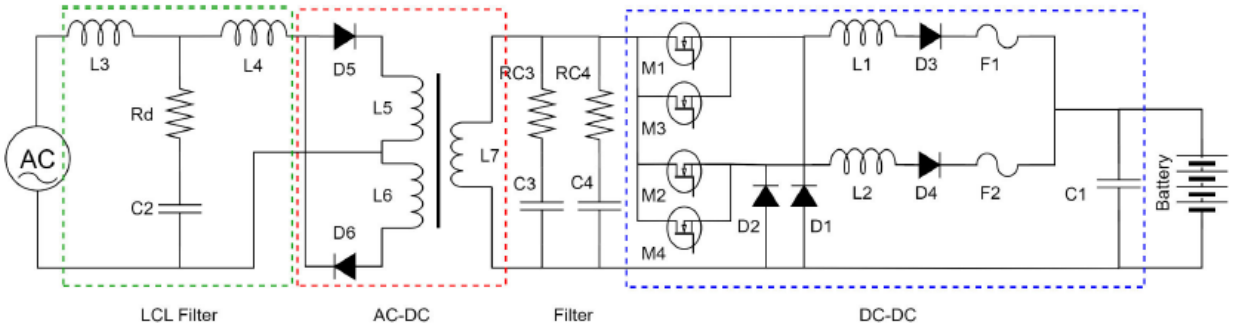

FIGURE 1. Proposed system.

INTERNATIONAL JOURNAL OF APPLIED SCIENCE ENGINEERING AND MANAGEMENT
ISSN 2454-9940
www.ijasem.org
Vol 19, Issue 2, 2025

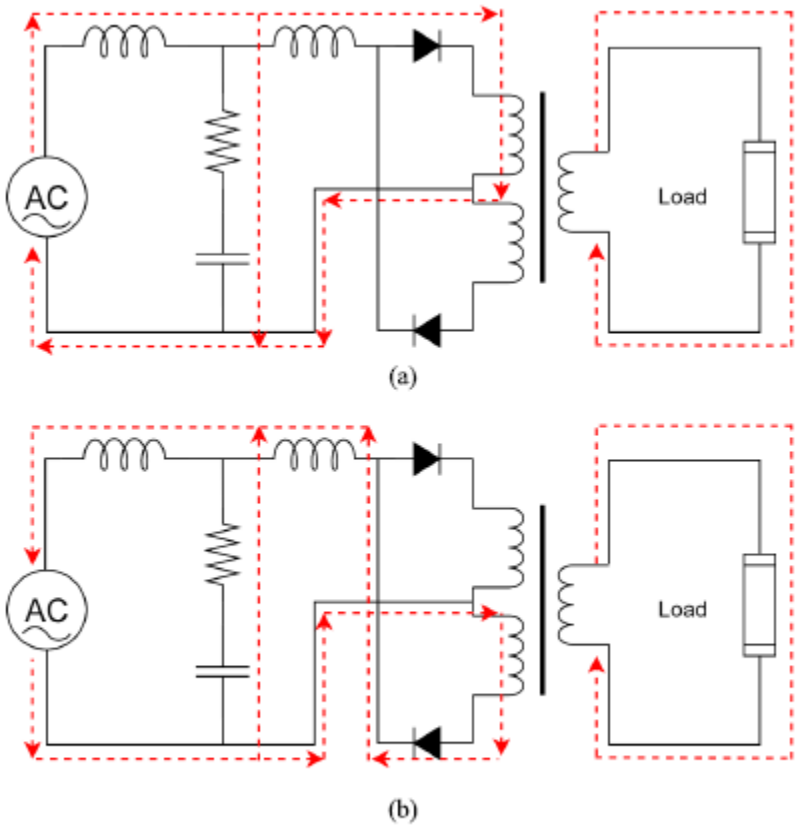

FIGURE 2. Working modes of the AC-DC converter with LCL filter (a) MODE ONE and (b) MODE TWO.

STEADY STATE ANALYSIS OF THE PROPOSED DC-DC SYSTEM

IDEAL CONDITION

For the sake of this examination, we will pretend that all the parts are perfect. Apart from that, has thought about fixing the duty cycle and switching frequency. An open-loop continuous conduction mode analysis is being performed on the system. The four modes of the proposed DC-DC converter have been covered in this discussion. FIRST MODE At the 0 < t < DTs time, the converter has analyzed. Currently, diodes 1 and 2 and MOSFETs 3 and 4 are in non-conduction modes, while MOSFETs 1 and 2 are in conduction mode. Inductors 1 and their left sides

INTERNATIONAL JOURNAL OF APPLIED SCIENCE ENGINEERING AND MANAGEMENT
ISSN 2454-9940
www.ijasem.org
Vol 19, Issue 2, 2025

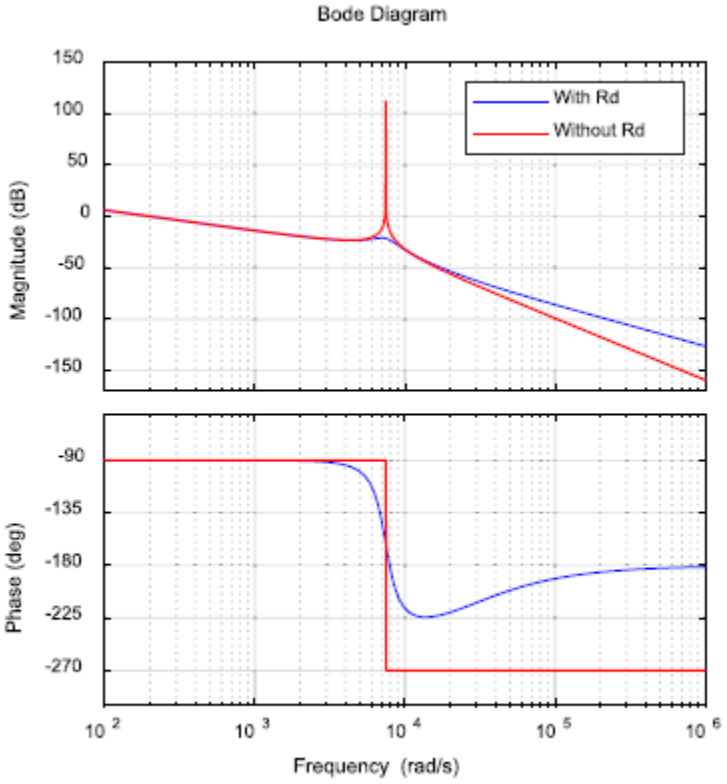

FIGURE 3. Bode plot of the designed LCL filter.

Figure 4(a) shows that two are now linked to the input source. Below, you can find the key equations of this mode.

$$v_{L1} = V_g - V_o \quad (7)$$

$$v_{L2} = V_g - V_o \quad (8)$$

$$\frac{d_{i_{L1}}}{dt} = \frac{Vg - V_0}{L1} \quad (9)$$

$$\frac{d_{i_{L2}}}{dt} = \frac{Vg - V_0}{L2} \quad (10)$$

$$i_{C1} = I_{L12} - I_o \quad (11)$$

2) MODE TWO

The converter is now being evaluated at the DTs \ t < Ts time interval. Now four of the MOSFETs are not conducting current. Now the first and second diodes are conducting current. Inductors 1 and 2's left sides are coupled to the

INTERNATIONAL JOURNAL OF APPLIED SCIENCE ENGINEERING AND MANAGEMENT
ISSN 2454-9940
www.ijasem.org
Vol 19, Issue 2, 2025

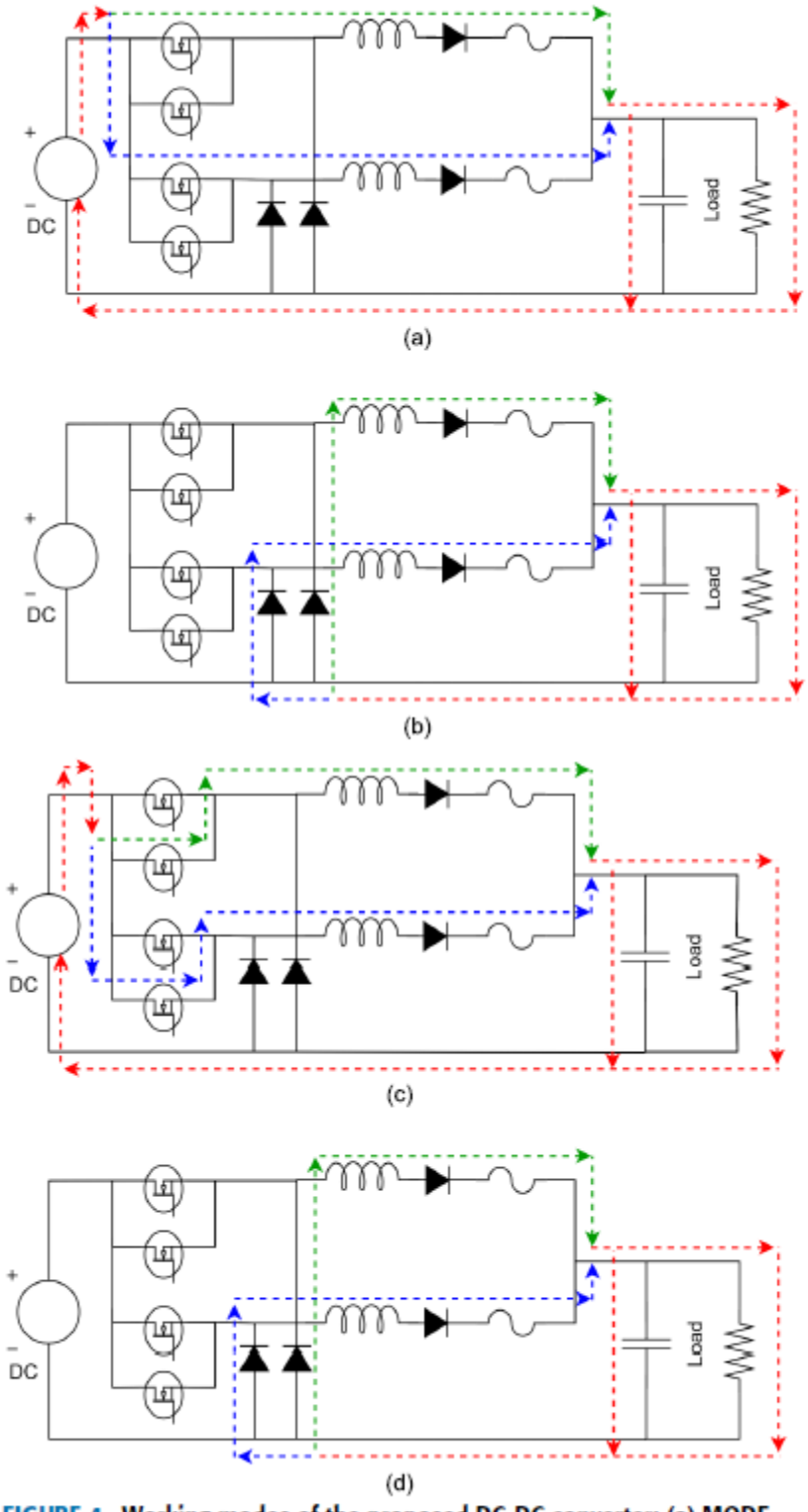

FIGURE 4. Working modes of the proposed DC-DC converter: (a) MODE ONE (b) MODE TWO (c) MODE THREE and (d) MODE FOUR.

ground and the circuit becomes Figure 4(b). The important equations in this mode are.

INTERNATIONAL JOURNAL OF APPLIED SCIENCE ENGINEERING AND MANAGEMENT
ISSN 2454-9940
www.ijasem.org
Vol 19, Issue 2, 2025

$$v_{L1} = -V_o \quad (12)$$

$$v_{L2} = -V_o \quad (13)$$

$$\frac{d_{i_{L1}}}{dt} = \frac{-V_0}{L1} \quad (14)$$

$$\frac{d_{i_{L2}}}{dt} = \frac{-V_0}{L2} \quad (15)$$

$$i_{C1} = I_{L12} - I_o \quad (16)$$

4) MODE FOUR

At the 2DTs < t < 2Ts time, the converter has now been examined. Once again, the first two diodes are conducting current, but this time four MOSFETs are in the non-conduction state. With the inductors' left sides reconnected to ground, the circuit changes to Figure 4(d). These equations are crucial.

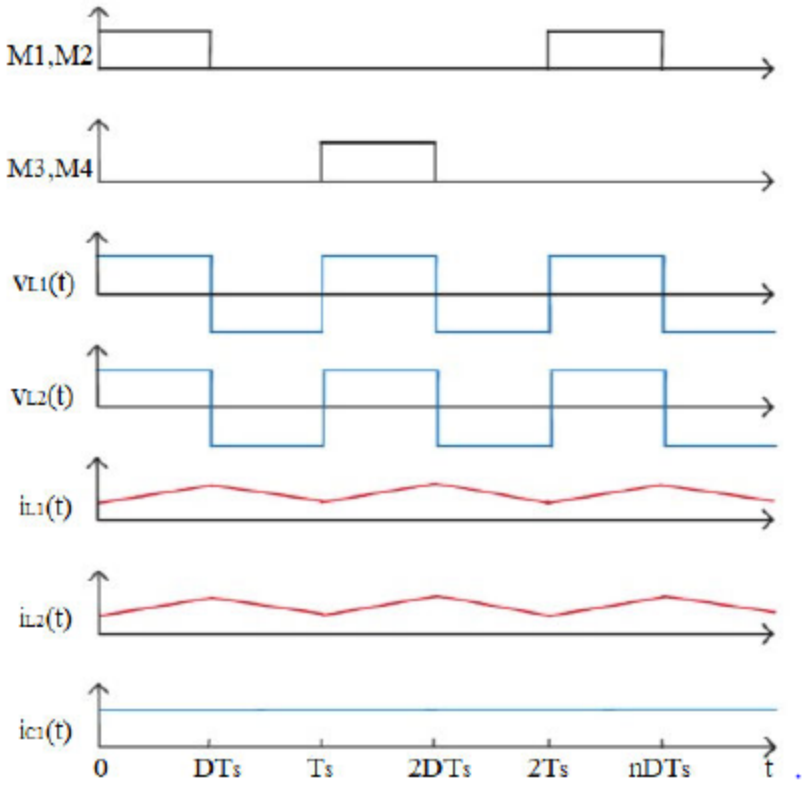

FIGURE 5. Proposed DC-DC converter waveforms: Switch or MOSFET one, two, three and four pulses (M1, M2, M3, M4), inductors voltage (v_{L1} and v_{L2}), inductors current (i_{L1} and i_{L2}) and capacitor current (i_{C1}).

INTERNATIONAL JOURNAL OF APPLIED SCIENCE ENGINEERING AND MANAGEMENT
ISSN 2454-9940
www.ijasem.org
Vol 19, Issue 2, 2025

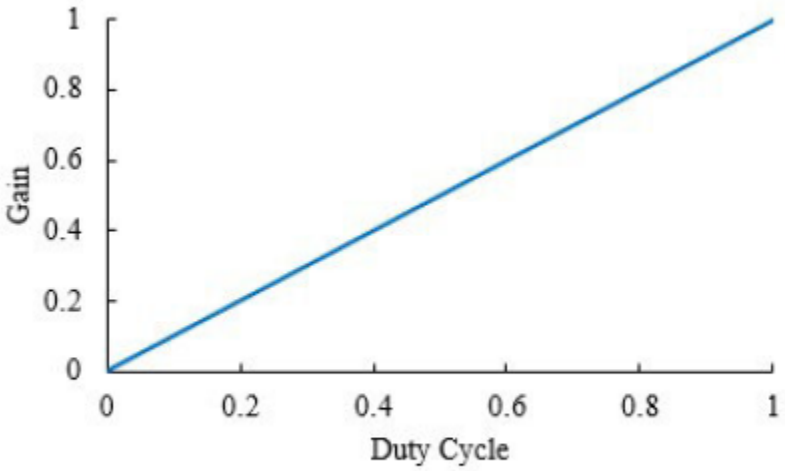

FIGURE 6. Ideal gain of the proposed DC-DC converter: G1 at 0 < t < Ts. G2 at 0 < t < Ts. G1 at Ts < t < 2Ts. G2 at Ts < t < 2Ts.

B. Deteriorating State With the assumption that all components are less than perfect, this study will focus on the SUP60020E MOSFET. The system has been evaluated in continuous conduction mode with the frequency and duty cycle assumed to remain constant. According to what was said before, the planned DC-DC system comprises four modes.

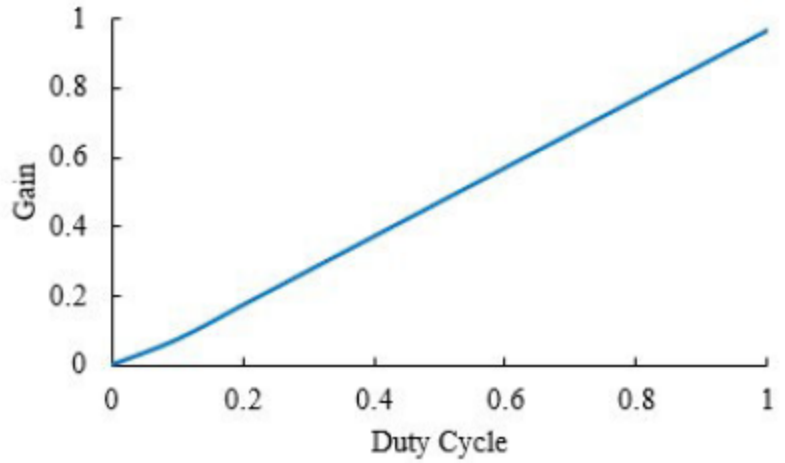

FIGURE 7. Non-Ideal gain of the proposed DC-DC converter: G1 at 0 < t < Ts. G2 at 0 < t < Ts. G1 at Ts < t < 2Ts. G2 at Ts < t < 2Ts.

INTERNATIONAL JOURNAL OF APPLIED SCIENCE ENGINEERING AND MANAGEMENT
ISSN 2454-9940
www.ijasem.org
Vol 19, Issue 2, 2025

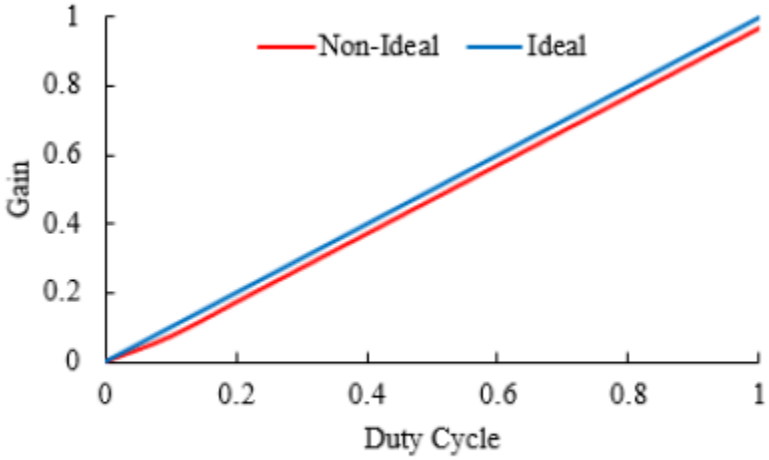

FIGURE 8. Ideal vs Non-Ideal gain comparison of the proposed DC-DC converter: G1 at 0 < t < Ts. G2 at 0 < t < Ts. G1 at Ts < t < 2Ts. G2 at Ts < t < 2Ts.

In terms of the less-than-idealities, the graph shows how they affect the DC conversion ratio. Even more so, the benefit grows in proportion to the duty cycle. As shown in Figure 8, a gain comparison was conducted under ideal and nonideal circumstances. It seems from the graph that the benefit is less in less-than-perfect circumstances compared to the ideal one.

DESIGN OF PROPOSED CLOSED LOOP CONTROLLER

In Figure 9, we can see the updated proportional integral (MPI) controller with logic closed loop functionality. Prior research has shown the outcome of the adjusted PI controller [25], [26]. This is the definition of the instantaneous intended output voltage.

$$\mathrm{Vref}\,(t) = \mathrm{nu}\,(t)$$

In accordance with equation 56, the sample and process block modifies this intended output voltage at runtime.

$$\mathrm{V'ref}\,(t) = \frac{n}{m}\mathrm{r}\,(t-0) - \frac{n}{m}\mathrm{r}\,(t-m)$$

where n is the battery output voltage and m is the settling time that is needed. Thereafter, the first PI block linked with the intended output current receives the result of comparing the actual output voltage with the changed desired output voltage. The second PI block receives the inverted output of the first and compares it to the real output current. Following the second PI block, the PWM modulator receives its output. Using the Zeigler-Nichols approach, the PI tuning for the first and second blocks has been completed. The output of the second PI and the Sawtooth block determine the frequency at which the PWM Generator block creates the necessary pulse. Following its generation, the pulse is sent to the logic block that regulates the MOSFETs. While MOSFETs three and four are not conducting during the first conduction phase, MOSFETs one and two are. Third and fourth MOSFETs conduct during the second conduction phase, but first and second do not. Following the steps outlined earlier, all MOSFETs remain in the nonconduction mode throughout the nonconduction time. Figure 10 provides a comprehensive flow diagram of the proposed closed loop system's prosecution.

PROPOSED SYSTEM RESULTS ANALYSIS

You may find a summary of the key parameters of the suggested system in Table 1. Figure 11 shows the results of a comparison between the traditional PI and the suggested control method. Based on the graph, it seems that the suggested control system computes quicker than the standard PI after 1st PI controller in terms of reaching steady

INTERNATIONAL JOURNAL OF APPLIED SCIENCE ENGINEERING AND MANAGEMENT
ISSN 2454-9940
www.ijasem.org
Vol 19, Issue 2, 2025

state, saving 96.98% of the time. Figure 11 shows the controller response as a result of the first PI current execution. So, this isn't the straight answer from the battery. In addition,

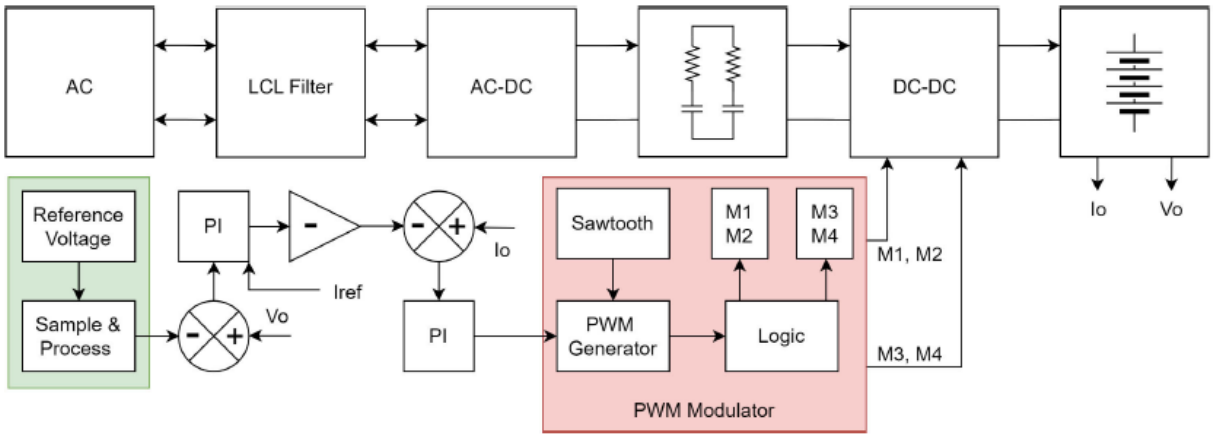

FIGURE 9. Block diagram of the closed loop proposed system.

TABLE 1. Parameters of the proposed system.

Parameters	Value
Source	Single phase AC (Grid)
Output voltage	54V
Output current	154A
Switching frequency	31kHz
DC inductor (L1, L2)	0.2mH
AC inductor (L3, L4)	2.47mH
Output capacitor (C1)	300uF
Input capacitor (C2)	14.5uF
Filter capacitor (C3, C4)	100uF

The lithium-ion battery model in MATLAB has been used for the simulation. Figure 9 displays the MATLAB Simulink-created system with the suggested technique for charging the lithium-ion battery from a single-phase ac grid. Figures 12–14 show the acquired findings from the simulation. While charging the lithium-ion battery, the findings demonstrate that the suggested system with the recommended approach maintained the voltage and current exactly as needed, with almost no overshoot. A settling time of 0.21 seconds was required to generate a charging current of up to about 152.1A. Figure 12 shows that the two-level rapid charging characteristics are satisfied when the battery voltage was maintained at around 53.3V and the state of charge went from 60% to 60.04% in about 1 second. This means that the charger would need roughly 17 minutes to charge the battery to 100%. While charging, the grid voltage and current were almost in phase, with a power factor of more than 0.90 and a total harmonic distortion (THD) of 0.46%, as shown in Figures 13 and 14, respectively.

POWER LOSS CALCULATION OF MOSFETS

It is necessary to calculate the power loss of MOSFETs in non-ideal circumstances in order to forecast the converter's dependability and efficiency with respect to the anticipated application. Figure 15 displays the control signal and consequences of each MOSFET in terms of voltage and current. The control pulses are M1, M2, M3, and

INTERNATIONAL JOURNAL OF APPLIED SCIENCE ENGINEERING AND MANAGEMENT
ISSN 2454-9940
www.ijasem.org
Vol 19, Issue 2, 2025

M4, whereas the voltage and current phenomena continuously shown by blue and red are M1p, M2p, M3p, and M4p, respectively. Power losses occur because MOSFET responses to control pulses are not immediate, as shown in Figure 15 [29]. There is some current flowing through MOSFETs 1 and 2 from t4 to t9, but the voltage is attenuated between t6 and t7 because neighboring MOSFETs 3 and 4 conduct at that period, minimizing leakage power loss; the process then repeats. At t2-t3 and t10-t11, the voltage across these two MOSFETs is reduced because MOSFETs 1 and 2 conduct, thereby minimizing the leakage power loss. From t5 to t8, the MOSFETs are in conduction mode; at other times, they are in non-conduction mode. The control signal that has been generated from the closed loop proposed control system divides the frequency and duty cycle of each MOSFET in half, as shown in Figure 15. As a result, each MOSFET experiences minimal conduction, switching, and leakage power losses. You can find out how much power each MOSFET loses overall by using equation 57.

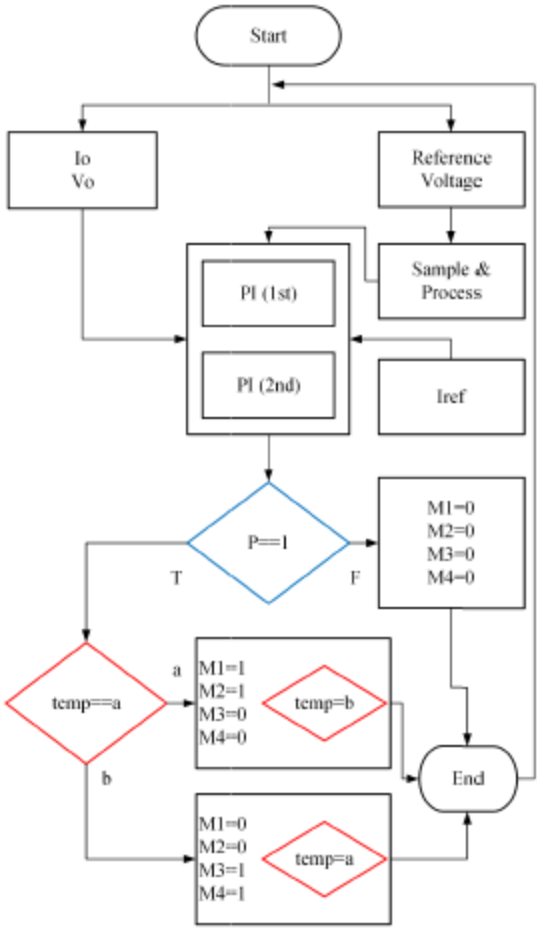

FIGURE 10. Flow chart of the proposed prosecution working principle of the closed loop proposed system.

INTERNATIONAL JOURNAL OF APPLIED SCIENCE ENGINEERING AND MANAGEMENT
ISSN 2454-9940
www.ijasem.org
Vol 19, Issue 2, 2025

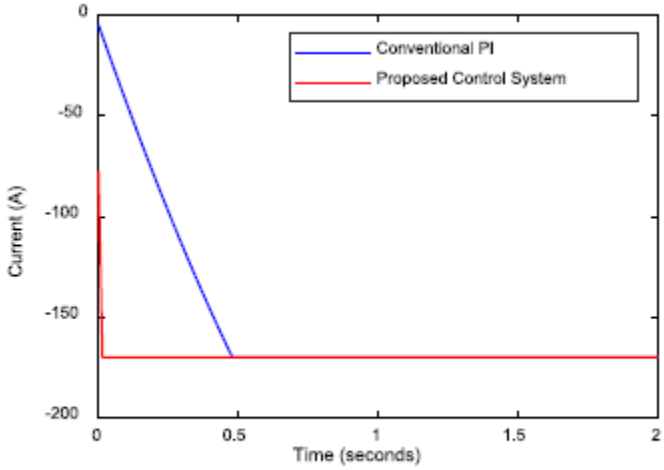

FIGURE 11. Simulated comparison between conventional PI and the proposed control system in terms of the current prosecution.

p_4 = Turn off delay time power loss
p_5 = Fall time power loss
p_6 = Leakage power loss.

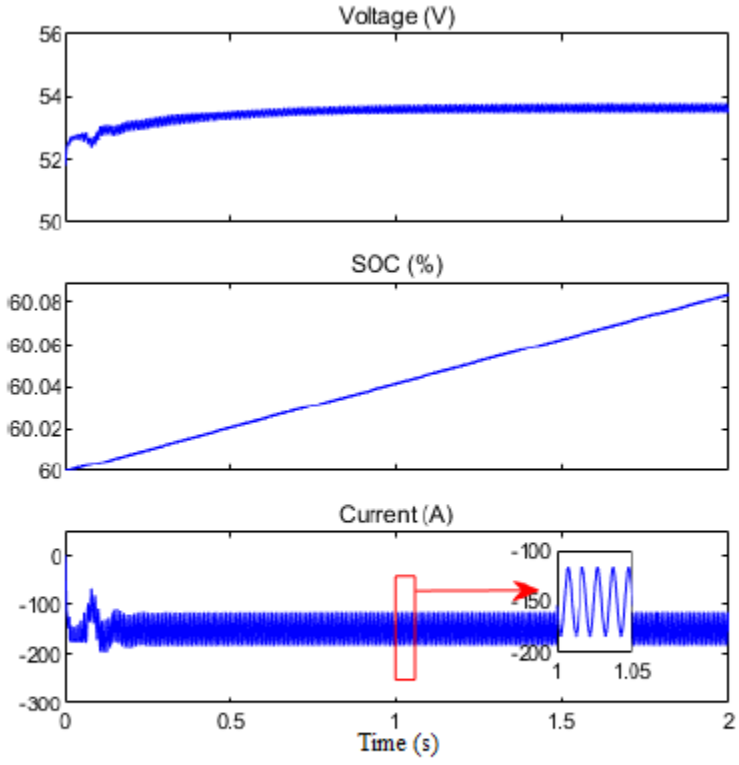

FIGURE 12. Simulated characteristics of battery voltage, soc and charging current under non-ideal condition of the proposed system with proposed prosecution.

INTERNATIONAL JOURNAL OF APPLIED SCIENCE ENGINEERING AND MANAGEMENT
ISSN 2454-9940
www.ijasem.org
Vol 19, Issue 2, 2025

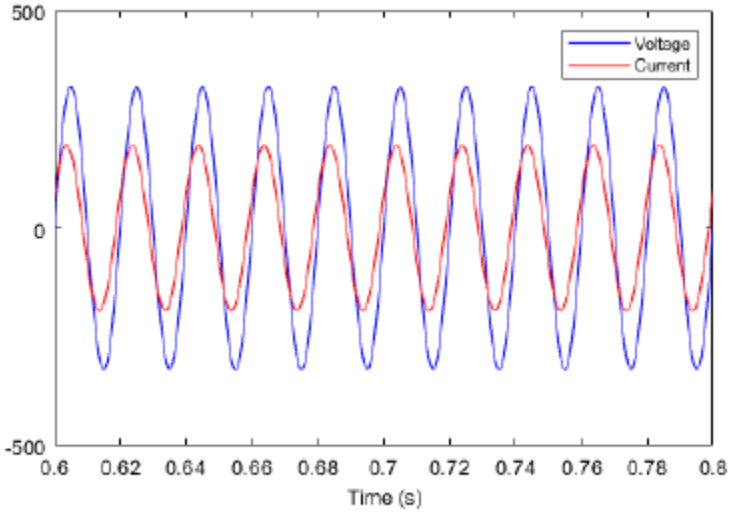

FIGURE 13. Simulated consequence of the grid voltage and current under non-ideal condition of the proposed system with proposed prosecution.

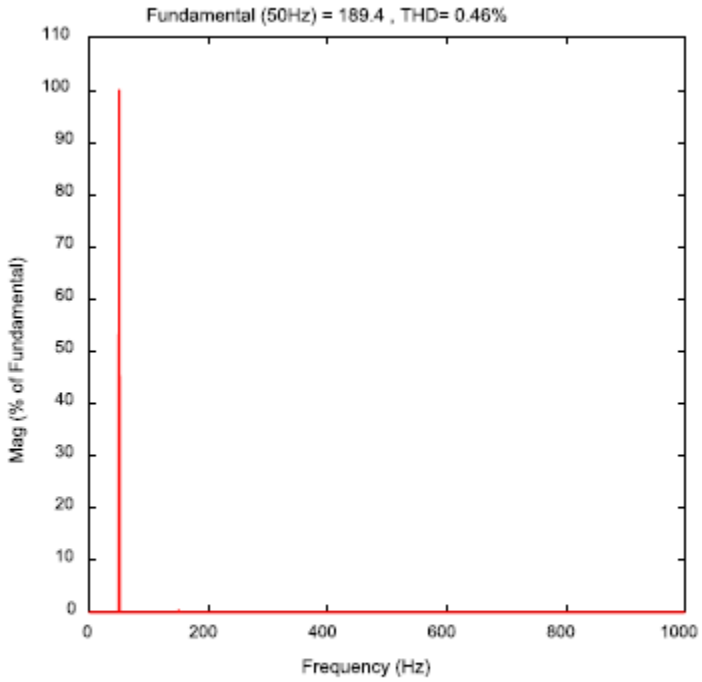

FIGURE 14. Simulated THD in terms of grid current under non-ideal condition of the proposed system with proposed prosecution.

INTERNATIONAL JOURNAL OF APPLIED SCIENCE ENGINEERING AND MANAGEMENT
ISSN 2454-9940
www.ijasem.org
Vol 19, Issue 2, 2025

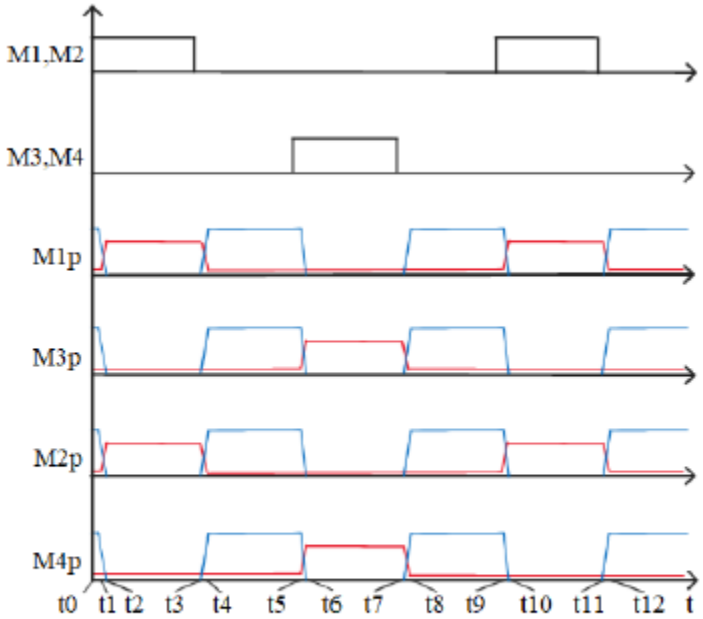

FIGURE 15. MOSFETs voltage and current waveforms of the proposed non-ideal DC-DC converter in terms of proposed prosecution.

The calculated power losses of MOSFETs are shown in Figures 16–19. From what we can see from these data, the MOSFETs start to dissipate spike power losses just after the prosecution begins. The power loss profiles of the four MOSFETs are almost similar. While charging the lithium-ion battery with a 152.1A charging current, each MOSFET produces a total power loss of 6.103W. Figure 20 shows the results of a power loss comparison between the reference system and the proposed system at the high-side MOSFET level [30]. Other than switching out the MOSFET control logic, both instances used the same closed-loop controller settings.

INTERNATIONAL JOURNAL OF APPLIED SCIENCE ENGINEERING AND MANAGEMENT
ISSN 2454-9940
www.ijasem.org
Vol 19, Issue 2, 2025

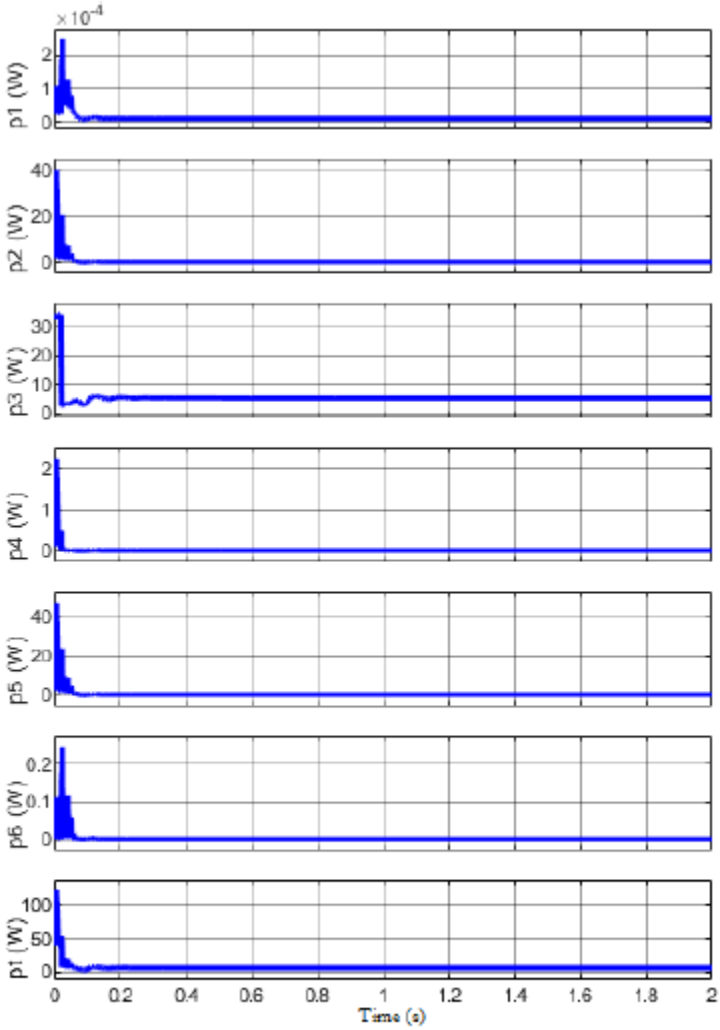

FIGURE 16. Simulated MOSFET one's power losses analysis of the proposed non-ideal converter in terms of proposed prosecution.

In contrast to the reference converter, which loses a lot of power on a single high-side MOSFET, the suggested converter loses less power on all of its high-side MOSFETs. The reference high-side MOSFET dissipates nearly 37.13W while charging the lithium-ion battery with 152.1A, which would increase the junction temperature of a MOSFET and shorten its life cycle. In contrast, the proposed system has a total power loss of about 6.103W for each high-side MOSFET. Figure 21 indicates that all power losses, except leakage, have been decreased. Leakage power loss is greater in the suggested converter than in the reference because each high-side MOSFET is in non-conduction mode for an extended period of time. But with only 83.6% power loss per high-side MOSFET, the suggested converter is a huge improvement.

MOSFET THERMAL ANALYSIS

The junction temperature of MOSFETs has been studied using the thermal conduction approach. The geometric electric field that flows via the MOSFET junction and

INTERNATIONAL JOURNAL OF APPLIED SCIENCE ENGINEERING AND MANAGEMENT
ISSN 2454-9940
www.ijasem.org
Vol 19, Issue 2, 2025

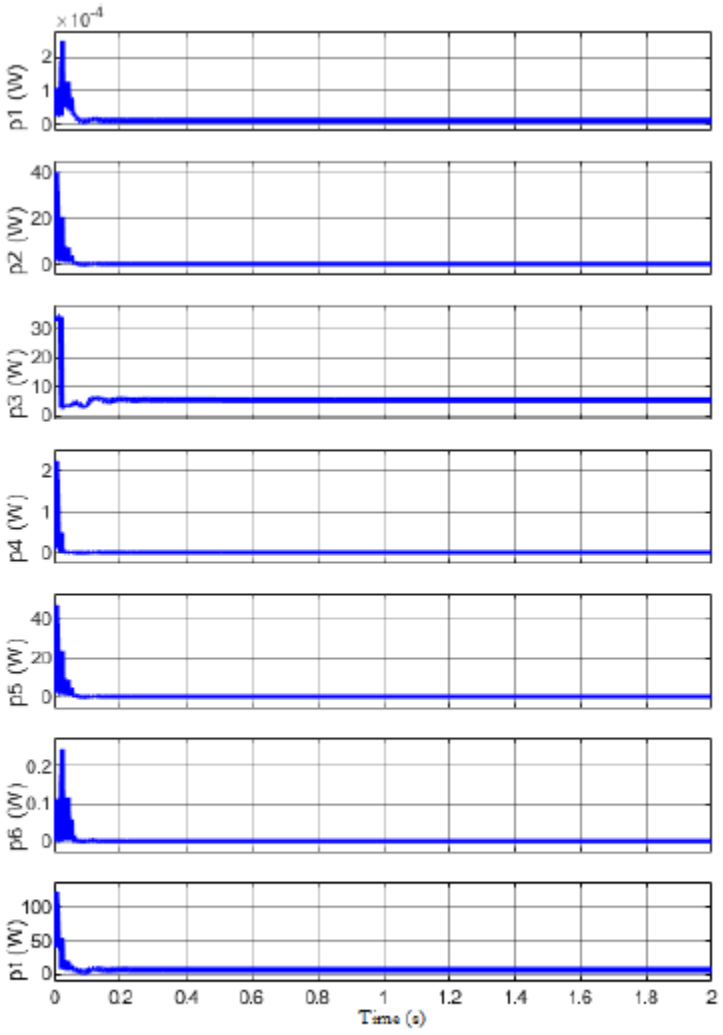

FIGURE 17. Simulated MOSFET two's power losses analysis of the proposed non-ideal converter in terms of proposed prosecution.

the heat sink has been expressed in equation 64.

$$T_j = P_t \times \left(R_{\theta ja} + R_{\theta sa} + R_{\theta cs} + R_{\theta jc}\right) + T_a$$

where

T_j = MOSFET junction temperature
P_t = MOSFET total power loss
$R_{\theta ja}$ = Junction to Air thermal conduction resistance
$R_{\theta sa}$ = Heat sink to Air thermal conduction resistance
$R_{\theta cs}$ = Case to Heat sink thermal conduction resistance
$R_{\theta jc}$ = Junction to Case thermal conduction resistance
T_a = Ambient temperature.

We have looked at three distinct modes that deal with the temperature at the MOSFET junction. MOSFETs that use convection cooling instead of an external heatsink (t j1). An external heatsink and natural cooling (t j2) are used in

MOSFETs. an external heatsink and forced cooling (t j3) MOSFET. An study of the exterior heatsink will be conducted by the RA-T2X-64E. The airflow has been set at room temperature and assumed to be continuous, except when discussing forced cooling at 500 feet per minute. For improved connection and isolation, mica has also been investigated between the exterior heatsink and MOSFET. Laboratory Evaluation of the System's Hardware Prototype We have successfully developed and tested a hardware prototype of the proposed dc-dc converter operating in open loop circumstances. Figure 40 illustrates the result. In order to confirm the outcome of the proposed system with the suggested prosecution, Table 2 provides the relevant factors. Figures 41 (a) and (b) show the prosecution pulses, as mentioned before. Figures 42 show the results of the MOSFETs with respect to the current and voltage. What has been described in the preceding sections. As a result of conduction and switching losses, the voltage drops to zero and the neighboring MOSFETs begin to conduct when the current drops below a certain threshold, reducing the leakage power loss to a minimum. The effect on the current through the inductors and the pulses of the MOSFETs is seen in Figures 43. The conduction loss is reduced because the neighboring MOSFETs conduct for the whole pulse, and each inductor current occurs even when there is a non-conduction period for one MOSFET.

TABLE 2. Parameters of the hardware testing.

Parameters	Value
Input voltage	15V
Switching frequency	15.5kHz
Duty Cycle	0.3
DC inductor (L1, L2)	0.6mH
Output capacitor (C1)	1000uF

Figure 44 shows the voltage and current plotted for the dc inductors. The inductor current grows with an incoming positive voltage and decreases with an outgoing negative voltage.

CONCLUSION

A high-gain DC-DC converter for electric vehicle charging applications based on a modified PI controller is proposed in this research. The relationship between input voltage, output voltage, and the prosecution is shown by the steady-state study of the proposed converter under both ideal and non-ideal situations. An examination of the MOSFETs' thermal performance and power loss reveals that the suggested procedure may lower the temperature and overall power loss of the devices. A well-designed DC and AC side inductor allows for efficient and cost-effective operation. The findings show that the temperature increase is within an acceptable range and that the planned inductors remain below the saturation area. The system is able to charge the lithium-ion battery with 152.1A while preserving overshoot and other parameters with the suggested converter and prosecution. In addition, we were able to attain a power factor of 90% and a total harmonic distortion (THD) of 0.46%. The dc-dc converter's frequency response verifies the system's stability in both ideal and non-ideal circumstances. The suggested system will outperform the traditional one in terms of reliability and operational efficiency, as confirmed by the examination of the MOSFETs' power loss and temperature profile.

REFERENCES

[1] M. R. Haque, S. Das, M. R. Uddin, M. S. I. Leon, and M. A. Razzak, ‘‘Performance evaluation of 1 kW asynchronous and synchronous buck converter-based solar-powered battery charging system for electric vehicles,’’ in *Proc. IEEE Region Symp. (TENSYMP)*, Jun. 2020, pp. 770–773, doi: 10.1109/TENSYMP50017.2020.9230833.
[2] M. R. Uddin, M. R. Uddin, K. F. I. Faruque, K. F. I. Faruque, P. Das, P. Das, K. M. Salim, and K. M. Salim, ‘‘An alternative PWM controlled high efficient solution for 60 V electric vehicle charging system to replace typical iron core charger: Technical performance assessment and comparison of efficiency,’’ in *Proc. IEEE Region Symp. (TENSYMP)*, Jun. 2020, pp. 312–315, doi: 10.1109/TENSYMP50017.2020.9231032.
[3] K. F. I. Faruque, M. R. Uddin, M. I. I. Sakib, and K. M. Salim, ‘‘Multiple outputs converter design for BMS integrated Li-ion battery charger appropriate for electric vehicle,’’ in *Proc. Int. Conf. Sci. Contemp. Technol. (ICSCT)*, Aug. 2021, pp. 1–5, doi: 10.1109/ICSCT53883.2021.9642568.

[4] S. Das, K. M. Salim, and D. Chowdhury, ‘‘A novel variable width PWM switching based buck converter to control power factor correction phenomenon for an efficacious grid integrated electric vehicle battery charger,’’ in *Proc. TENCON IEEE Region Conf.*, Nov. 2017, pp. 262–267, doi: 10.1109/TENCON.2017.8227873.
[5] S. Das, K. M. Salim, D. Chowdhury, and M. M. Hasan, ‘‘Inverse sinusoidal pulse width modulation switched electric vehicles’ battery charger,’’ *Int. J. Electr. Comput. Eng. (IJECE)*, vol. 9, no. 5, p. 3344, Oct. 2019.
[6] A. Alassi, A. Al-Aswad, A. Gastli, L. B. Brahim, and A. Massoud, ‘‘Assessment of isolated and non-isolated DC–DC converters for mediumvoltage PV applications,’’ in *Proc. 9th IEEE-GCC Conf. Exhib. (GCCCE)*, May 2017, pp. 1–6, doi: 10.1109/IEEEGCC.2017.8448079.
[7] S. Das, M. R. Haque, and M. A. Razzak, ‘‘Development of one-kilowatt capacity single phase pure sine wave off-grid PV inverter,’’ in *Proc. IEEE Region Symp. (TENSYMP)*, Jun. 2020, pp. 774–777, doi: 10.1109/TENSYMP50017.2020.9230909.
[8] M. M. Faruk, N. T. Khan, and M. A. Razzak, ‘‘Analysis of the impact of EV charging on THD, power factor and power quality of distribution grid,’’ in *Proc. Innov. Power Adv. Comput. Technol. (i-PACT)*, Nov. 2021, pp. 1–6, doi: 10.1109/i-PACT52855.2021.9697024.
[9] A. Kumar and P. Kumar, ‘‘Power quality improvement for grid-connected PV system based on distribution static compensator with fuzzy logic controller and UVT/ADALINE-based least mean square controller,’’ *J. Modern Power Syst. Clean Energy*, vol. 9, no. 6, pp. 1289–1299, 2021, doi: 10.35833/MPCE.2021.000285.
[10] V. Nagamalleswari, S. R. Arya, S. Mallikharjun, and G. Sridhar, ‘‘Improvement in power quality for distribution system using momentum algorithm,’’ in *Proc. IEEE 2nd Int. Conf. Sustain. Energy Future Electric Transp. (SeFeT)*, Aug. 2022, pp. 1–5, doi: 10.1109/SeFeT55524.2022.9909013.
[11] F. Zheng andW. Zhang, ‘‘Long term effect of power factor correction on the industrial load: A case study,’’ in *Proc. Australas. Universities Power Eng. Conf. (AUPEC)*, Nov. 2017, pp. 1–5, doi: 10.1109/AUPEC.2017.8282382.
[12] J. Ye and H. B. Gooi, ‘‘Phase angle control based three-phase DVR with power factor correction at point of common coupling,’’ *J. Modern Power Syst. Clean Energy*, vol. 8, no. 1, pp. 179–186, 2020, doi: 10.35833/MPCE.2018.000428.
[13] S. S. Sayed and A. M. Massoud, ‘‘Review on state-of-the-art unidirectional non-isolated power factor correction converters for short-/long-distance electric vehicles,’’ *IEEE Access*, vol. 10, pp. 11308–11340, 2022, doi: 10.1109/ACCESS.2022.3146410.
[14] K. Cao, X. Liu, M. He, X. Meng, and Q. Zhou, ‘‘Active-clamp resonant power factor correction converter with output ripple suppression,’’ *IEEE Access*, vol. 9, pp. 5260–5272, 2021, doi: 10.1109/ACCESS.2020.3048012.
[15] J.-Y. Lin, P.-H. Liu, H.-Y. Yueh, and Y.-F. Lin, ‘‘Design of boost-type power factor correction with stepped air-gap ferrite inductor for peakpower- load condition,’’ *IEEE Access*, vol. 10, pp. 57655–57664, 2022, doi: 10.1109/ACCESS.2022.3179401.
[16] S. Abdelhady, A. Osama, A. Shaban, and M. Elbayoumi, ‘‘A realtime optimization of reactive power for an intelligent system using genetic algorithm,’’ *IEEE Access*, vol. 8, pp. 11991–12000, 2020, doi: 10.1109/ACCESS.2020.2965321.
[17] G. Zhang, J. Zeng, S. S. Yu,W. Xiao, B. Zhang, S.-Z. Chen, and Y. Zhang, ‘‘Control design and performance analysis of a double-switched LLC resonant rectifier for unity power factor and soft-switching,’’ *IEEE Access*, vol. 8, pp. 44511–44521, 2020, doi: 10.1109/ACCESS.2020.2978030.
[18] L. Sarker, M. Nazir, and M. A. Razzak, ‘‘Harmonics reduction and power factor correction for electric vehicle charging system,’’ in *Proc. Innov. Power Adv. Comput. Technol. (i-PACT)*, Nov. 2021, pp. 1–6, doi: 10.1109/i-PACT52855.2021.9696738.
[19] M. A. Razzak, S. B. Afzal, and M. M. Shabab, ‘‘A π-CLCL type immittance converter for constant current and dynamic load applications,’’ *Int. J. Electr. Comput. Eng. (IJECE)*, vol. 4, no. 5, pp. 679–690, Oct. 2014, doi: 10.11591/ijece.v4i5.5957.
[20] R. N. Beres, X. Wang, F. Blaabjerg, M. Liserre, and C. L. Bak, ‘‘Optimal design of high-order passive-damped filters for grid-connected applications,’’ *IEEE Trans. Power Electron.*, vol. 31, no. 4, pp. 2083–2098, Mar. 2016, doi: 10.1109/TPEL.2015.2441299.